PHYSICAL REVIEW D **97,** 022004 (2018)

# Silicon nitride films fabricated by a plasma-enhanced chemical vapor deposition method for coatings of the laser interferometer gravitational wave detector

Huang-Wei Pan, Ling-Chi Kuo, Shu-Yu Huang, Meng-Yun Wu, Yu-Hang Juang, Chia-Wei Lee, Hsin-Chieh Chen, Ting Ting Wen, and Shiuh Chao*

*Institute of Photonics Technologies, National Tsing Hua University,*
*Hsinchu 30013, Taiwan, Republic of China*

(Received 31 October 2017; published 24 January 2018)

Silicon is a potential substrate material for the large-areal-size mirrors of the next-generation laser interferometer gravitational wave detector operated in cryogenics. Silicon nitride thin films uniformly deposited by a chemical vapor deposition method on large-size silicon wafers is a common practice in the silicon integrated circuit industry. We used plasma-enhanced chemical vapor deposition to deposit silicon nitride films on silicon and studied the physical properties of the films that are pertinent to application of mirror coatings for laser interferometer gravitational wave detectors. We measured and analyzed the structure, optical properties, stress, Young's modulus, and mechanical loss of the films, at both room and cryogenic temperatures. Optical extinction coefficients of the films were in the $10^{-5}$ range at 1550-nm wavelength. Room-temperature mechanical loss of the films varied in the range from low $10^{-4}$ to low $10^{-5}$ within the frequency range of interest. The existence of a cryogenic mechanical loss peak depended on the composition of the films. We measured the bond concentrations of N—H, Si—H, Si—N, and Si—Si bonds in the films and analyzed the correlations between bond concentrations and cryogenic mechanical losses. We proposed three possible two-level systems associated with the N—H, Si—H, and Si—N bonds in the film. We inferred that the dominant source of the cryogenic mechanical loss for the silicon nitride films is the two-level system of exchanging position between a $H^+$ and electron lone pair associated with the N—H bond. Under our deposition conditions, superior properties in terms of high refractive index with a large adjustable range, low optical absorption, and low mechanical loss were achieved for films with lower nitrogen content and lower N—H bond concentration. Possible pairing of the silicon nitride films with other materials in the quarter-wave stack is discussed.

DOI: 10.1103/PhysRevD.97.022004

## I. INTRODUCTION

With the first detection of gravitational waves by the advanced Laser Interferometer Gravitational Wave Observatory (advanced LIGO) [1], development of the detector technologies is now focused on increasing the sensitivity of the current detectors by a factor of approximately three in the coming three to five years [2] and to develop the technologies toward the next-generation detector operated in cryogenics.

Brownian thermal noise of the mirror coatings is the dominant noise source in the current detector at frequencies near 100 Hz, where the detector is the most sensitive. Thermal noise is related to mechanical dissipation through the fluctuation-dissipation theorem [3]. Reducing the room-temperature and cryogenic mechanical loss of the coating materials is therefore crucial for enhancing the sensitivity of the current and future detectors. The detector's mirror coatings are composed of two thin-film materials with high and low refractive indices alternately deposited on a substrate; each layer has one quarter-wavelength optical thickness. The diameter of the mirror is 34 cm for the current detector [4] and is likely to be ≈40 cm [2] or larger [5] for the next-generation detector. Uniformly depositing thin films on a large-area substrate is challenging. Ion-beam sputter (IBS) has been used to deposit coatings on fused silica substrates 34 cm in diameter for the current detector because of its capability of producing denser and hence higher-refractive-index films, but the line-of-sight impinging nature of the deposited atoms causes uniformity problems, and sophisticated deposition techniques must be employed [6,7] to achieve the stringent thickness uniformity requirement. Amorphous $Ti:Ta_2O_5$ and $SiO_2$ thin films deposited by the IBS method were used as the high- and low-index materials for the coatings of the current detector [4]. However, both materials suffered from mechanical loss peaks at cryogenic temperatures that

---

*Corresponding author.
schao@ee.nthu.edu.tw

hinder their application as the coatings of the next-generation detector operated in cryogenics [8,9].

Silicon, because of its low cryogenic mechanical loss, is a potential candidate for the mirror substrate of the future detector [10]. Current semiconductor integrated circuit (IC) technology is sufficiently mature for processing large-size silicon wafers up to 18 inches in diameter, which is larger than the mirror size of the next-generation detector. Thin-film materials such as silicon nitride have been developed for coatings on large-size silicon wafers for various purposes in IC applications. The chemical vapor deposition (CVD) method is the most common thin-film deposition method for silicon IC applications, and good uniformity of the CVD coatings on large-size wafers is more easily achieved than the physical vapor deposition methods such as IBS because of its nature of gas-phase interaction and condensation. It was reported that the cryogenic mechanical loss of the silicon nitride film deposited by the low-pressure CVD (LPCVD) method was particularly low [11]. However, the measured frequency was ≈1.5 MHz, which is far beyond the frequency range of our interest. Therefore, we were motivated to study the silicon nitride film deposited by the CVD method for the purpose of low mechanical loss mirror coatings of the laser interferometer gravitational wave detector. An immediate foreseeable advantage is that the CVD process is favorable for achieving good uniformity on large-size silicon mirror substrates.

In this paper, we report the results of measurements and analysis of physical properties, in particular, the room-temperature and the cryogenic mechanical loss, which are pertinent to the application for coatings of the gravitational wave detector for the amorphous silicon nitride films deposited by using the plasma-enhanced CVD (PECVD) method. Two-level systems (TLS) in the silicon nitride film are proposed and analyzed with respect to the cryogenic mechanical loss. Possible materials that can be paired with the silicon nitride films for the mirror coatings of the future detector are also discussed.

## II. FABRICATION AND COMPOSITION

### A. Fabrication

We used the PECVD method to fabricate silicon nitride films on silicon substrates. In this method, chemical reactions between the precursors are activated near the heated substrate surface, and the product condenses on the substrate to form the film. Radio frequency (RF) power is introduced to generate plasma of the precursors so that the chemical reactions can proceed between the free radicals of the precursors at a lower substrate temperature to avoid the drawbacks of high-temperature processes such as LPCVD. A schematic of our deposition chamber is shown in Fig. 1. The precursors were silane ($SiH_4$) and ammonia ($NH_3$) gases; nitrogen was used as the carrier gas. RF power at 13.56 MHz was fed into the chamber.

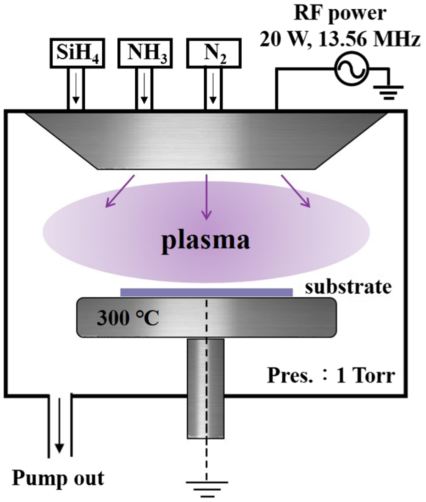

FIG. 1. Schematic diagram of plasma-enhanced chemical vapor deposition chamber.

The silicon nitride condensate in the PECVD process is seldom stoichiometric, and usually contains hydrogen. It is conventionally represented as $SiN_xH_y$. The composition of silicon nitride and hence its physical properties depend in a complicated way on various process parameters as well as the deposition rate [12–14]. In our experiment, $NH_3$ and $SiH_4$ were fed in at various flow-rate ratios to produce films with different compositions. The nitrogen carrier gas was fed in at a constant flow rate of 980 sccm. The total pressure in the chamber was held constant at 1 Torr. The RF power was fixed at 20 W and the substrate temperature was held at 300°C.

The substrates were (100) silicon in the form of a cantilever or other shapes. To avoid edge effects that produce uneven plasma distribution and hence uneven thickness and composition of the films, the substrates were mosaicked in a large silicon wafer during the PECVD process.

### B. Composition

Five samples of different $NH_3$ to $SiH_4$ flow-rate ratios (15∶45, 22∶38, 30∶25, 45∶15, and 48∶8 in units of sccm) were fabricated. The atomic ratio of nitrogen to silicon, $N_N/N_{Si}$, in the films was determined by using x-ray photoelectron spectroscopy (XPS). Bond concentrations were determined by using Fourier transform infrared spectroscopy (FTIR). The FTIR absorption spectra of the five samples are shown in Fig. 2. Notice that the Si─O bond existed only on the surface but not in the film, as was revealed by the XPS depth profile; therefore, it is disregarded from the following discussion. The bond concentration, $N$, is given as [15]

$$N = A \int \frac{a}{w} dw,$$

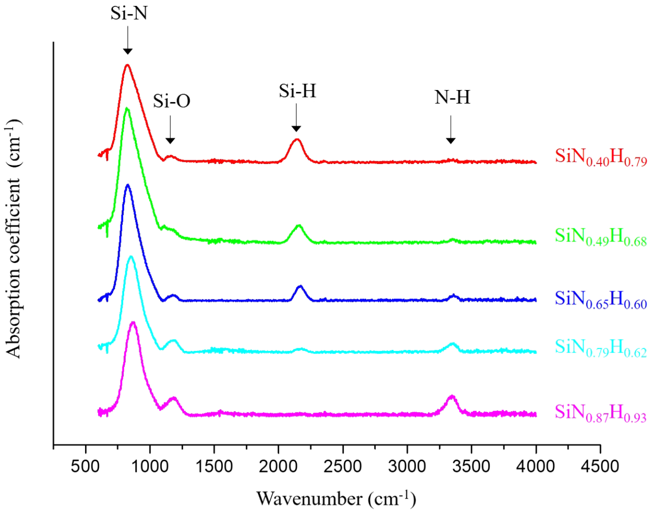

FIG. 2. IR absorption coefficient for Si—N, Si—O, Si—H, and N—H bonds of the silicon nitride films.

where $\alpha$ is the absorption coefficient, $w$ is the wave number, and $A$ is the proportional constant for the particular bond, which can be obtained from the calibrated values in the references. The $A$ values for the Si—H and N—H bonds from independent references were consistent at $1.4 \times 10^{20}$ and $2.8 \times 10^{20}$, respectively [16–18]. The concentration of Si—H and N—H bonds, $N_{\text{Si–H}}$ and $N_{\text{N–H}}$, can therefore be obtained confidently. However, the $A$ values for the Si—N bond varied by 1 order of magnitude in the literature [18–20]; thus, it must be obtained by other reliable means, described as follows.

Because hydrogen is connected only to either Si or N, the hydrogen atomic concentration can be expressed as

$$N_{\text{H}} = N_{\text{Si–H}} + N_{\text{N–H}}.$$

The mass density of the film $\rho$ is given as

$$\rho = M_{\text{Si}} N_{\text{Si}} + M_{\text{N}} N_{\text{N}} + M_{\text{H}} N_{\text{H}},$$

where $M_{\text{Si}}$, $M_{\text{N}}$, and $M_{\text{H}}$ are the mass of the silicon, nitrogen, and hydrogen atoms, respectively. We obtained the mass density of the film by measuring the difference in weight before and after coating and dividing by the volume of a film with known thickness and area. With the Si-to-N atomic ratio from XPS, the absolute value of Si and N concentration, $N_{\text{Si}}$ and $N_{\text{N}}$, can thus be obtained.

The nitrogen concentration can be expressed as

$$N_{\text{N}} = \frac{1}{3} N_{\text{Si–N}} + \frac{1}{3} N_{\text{N–H}} + \frac{2}{3} N_{\text{N–N}} + \frac{1}{3} N_{\text{N–}},$$

where $N_{\text{N–N}}$ and $N_{\text{N–}}$ are the concentration of the N—N bond and nitrogen dangling bond, respectively. It was reported that the bonding energy of the N—N bond is much lower than that of the Si—N and N—H bonds [21], and the concentration of the N—N bond was reported to be much lower than that of the Si—N and N—H bonds for films deposited by various CVD methods and conditions [22]; therefore we believe that $N_{\text{N–N}}$ can be neglected in our case. It was also reported that $N_{\text{N–}}$ and concentration of Si dangling bond, $N_{\text{Si–}}$, in films deposited by various methods were 3–4 orders of magnitude lower than that of the $N_{\text{Si–N}}$ and $N_{\text{N–H}}$ [18,21,23]; therefore, $N_{\text{N–}}$ can also be neglected in the equation. The concentration of Si—N bonds, $N_{\text{Si–N}}$, can therefore be obtained through the previous equation by substituting in the known $N_{\text{N}}$ and $N_{\text{N–H}}$ values.

The silicon concentration can be expressed as

$$N_{\text{Si}} = \frac{1}{4} N_{\text{Si–N}} + \frac{1}{4} N_{\text{Si–H}} + \frac{2}{4} N_{\text{Si–Si}} + \frac{1}{4} N_{\text{Si–}}.$$

$N_{\text{Si–}}$ is negligible according to the argument in the previous paragraph. Therefore, the concentration of Si—Si bonds, $N_{\text{Si–Si}}$, can be obtained by substituting the known $N_{\text{Si}}$, $N_{\text{Si–H}}$, and $N_{\text{Si–N}}$ values in the equation.

The results of the atomic concentrations of Si, N, and H, and bond concentrations of Si—N, Si—H, N—H, and Si—Si for the five silicon nitride thin films are listed in Table I and plotted in Fig. 3.

TABLE I. Atomic concentrations of Si, N, and H, and bond concentrations of Si—N, Si—H, N—H, and Si—Si for the five silicon nitride films with different compositions and densities fabricated by varying the $NH_3/SiH_4$ flow-rate ratio.

| $NH_3/SiH_4$ |  | Density | $N_{\text{Si}}$ | $N_{\text{N}}$ | $N_{\text{H}}$ | $N_{\text{Si–N}}$ | $N_{\text{Si–H}}$ | $N_{\text{N–H}}$ | $N_{\text{Si–Si}}$ |
|---|---|---|---|---|---|---|---|---|---|
| (sccm) | Composition | (g/cm$^3$) | ($10^{21}$/cm$^3$) |  |  |  |  |  |  |
| 15/45 | $SiN_{0.40}H_{0.79}$ | $2.00 \pm 0.03$ | 34.90 | 13.96 | 27.51 | 39.69 | 25.32 | 2.19 | 37.30 |
| 22/38 | $SiN_{0.49}H_{0.68}$ | $2.18 \pm 0.03$ | 36.79 | 18.03 | 24.83 | 50.68 | 21.43 | 3.40 | 37.52 |
| 30/25 | $SiN_{0.65}H_{0.60}$ | $2.13 \pm 0.02$ | 33.97 | 22.08 | 20.29 | 59.13 | 13.18 | 7.11 | 31.78 |
| 45/15 | $SiN_{0.79}H_{0.62}$ | $2.14 \pm 0.03$ | 32.38 | 25.58 | 20.00 | 62.83 | 6.08 | 13.92 | 30.31 |
| 48/8 | $SiN_{0.87}H_{0.93}$ | $2.10 \pm 0.03$ | 30.67 | 26.68 | 28.63 | 53.51 | 2.09 | 26.54 | 33.54 |

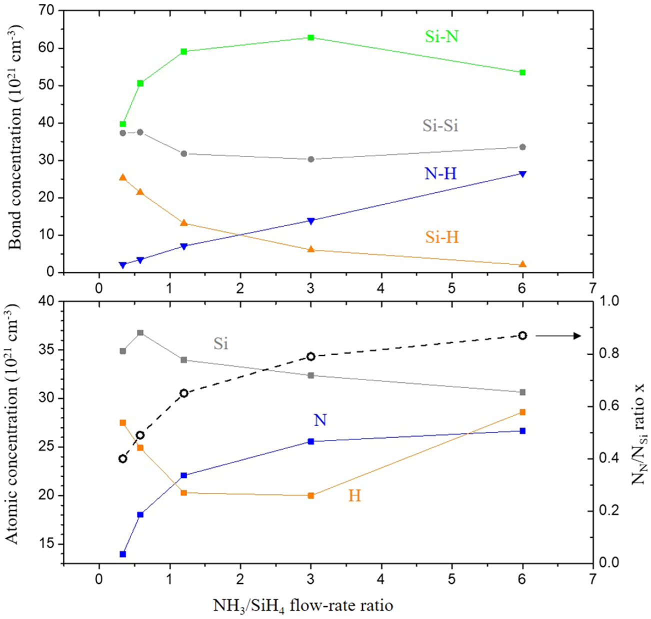

FIG. 3. Bond concentration for Si—N, Si—Si, N—H, and Si—H bonds (upper plot) and atomic concentration for Si, N, and H (lower plot) versus $NH_3/SiH_4$ flow-rate ratio for the five samples in Table I.

## III. MATERIAL PROPERTIES OF THE SILICON NITRIDE FILMS

### A. Structure

Figure 4 shows transmission electron microscope (TEM) images of the silicon nitride films of different compositions. It is clear that the structure of the films was amorphous as confirmed by the diffused electron diffraction patterns in the insets of Fig. 4. Similar results were reported [24,25] for the PECVD silicon nitride films.

### B. Optical properties

We used an ellipsometer (J. A. Woollam model M2000) to measure the dispersion of refractive index and extinction coefficient of the films. The Tauc-Lorentz model, developed for amorphous semiconductor materials, was used for fitting [26,27], and the energy band gap was also obtained. Figure 5 shows the results of the refractive index and extinction coefficient for the silicon nitride films of five different compositions. Energy band gaps are shown in Fig. 6. It is clear that both the refractive index and extinction coefficient decreased and the energy band gap increased with increasing nitrogen content. Above ≈600 nm, the extinction coefficient of all films dropped below the detection limit of the instrument, which is $\approx 10^{-3}$.

A photothermal common path interferometer (PCI; SPTS Model PCI-03) [28] was then used to measure the low-level absorption of the films at a wavelength of 1550 nm. The films were coated on the fused silica substrate for PCI measurement. Absorbance of the samples was measured and the extinction coefficients $\kappa$ of the films were obtained by using thin-film interference software to fit the measured absorbance with the known refractive indices and thicknesses of the films, assuming that the optical scattering was negligible. The absorption coefficient $\alpha$ was obtained from $\kappa$ by the simple conversion $\alpha = 4\pi\kappa/\lambda$. Films with five different compositions were measured by PCI; the results are shown in Table II, and the extinction coefficients are plotted in Fig. 6.

Figure 6 shows the refractive index for 1064 and 1550 nm wavelength, energy band gap, and extinction coefficient for 1550 nm versus $NH_3/SiH_4$ flow-rate ratio of the silicon nitride films. The former wavelength is the laser wavelength of the current advanced-LIGO detector, and the latter is the candidate wavelength for the next-generation detector. The refractive index of the silicon nitride varied from 2.30 to 1.78 for 1064 nm and from 2.28 to 1.78 for 1550 nm, indicating that the films could be served as either a high- or low-index layer in the multilayer high reflector structure. Extinction coefficients were in the $10^{-5}$ range and increased with increasing energy band gap, which implies that the PECVD silicon nitride films with larger energy gaps must have long band tails extended deeper into the band gap. The long band tail is likely to be of the

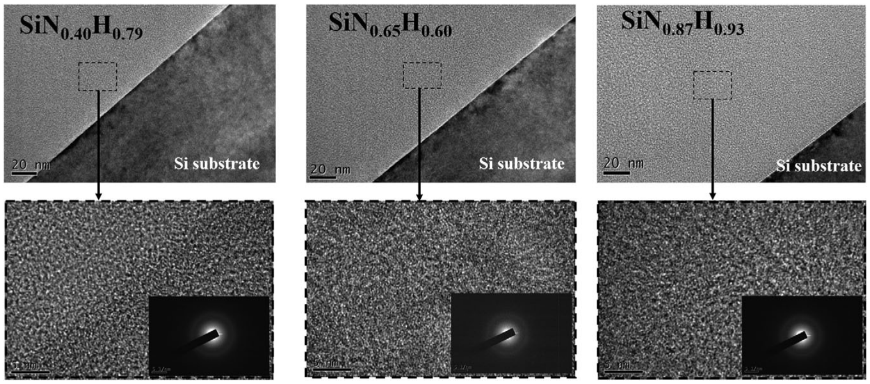

FIG. 4. TEM images and electron diffraction patterns for silicon nitride films with different compositions.

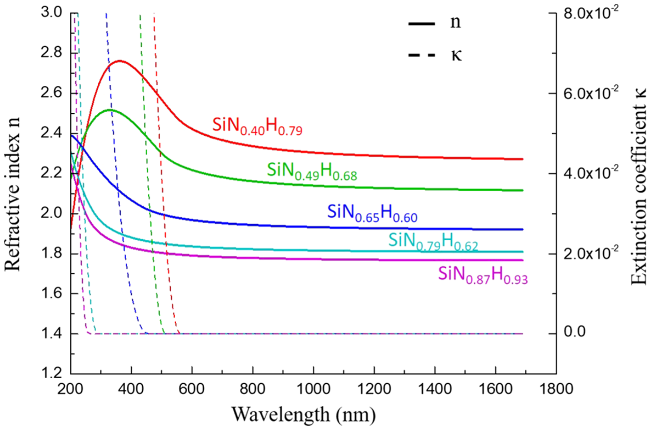

FIG. 5. Refractive indices and extinction coefficients spectra of silicon nitride films measured by ellipsometer.

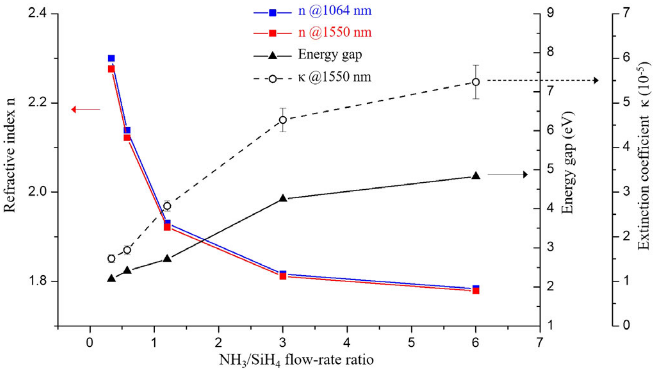

FIG. 6. Refractive indices at 1064 and 1550 nm and energy gaps versus $NH_3/SiH_4$ flow-rate ratio.

Urbach type for an amorphous structure [29–31] and originated from various electronic trap states deep in the band of the film material. The optical absorptions of the as-deposited silicon nitride films reported here are much lower than those of the IBS as-deposited amorphous silicon films [32,33], which is a potential high-index film for the coatings of the future detector.

## C. Stress

TABLE II. Thickness, absorbance, extinction coefficient $\kappa$, and absorption coefficient $\alpha$ at 1550 nm for silicon nitride samples.

| Samples | Thickness (nm) | Absorbance (ppm) | $\kappa$ $(10^{-5})$ | $\alpha$ $(\mathrm{cm}^{-1})$ |
|---|---|---|---|---|
| $SiN_{0.40}H_{0.79}$ | 492.6 | $46.7 \pm 3.1$ | $1.51 \pm 0.09$ | $1.22 \pm 0.08$ |
| $SiN_{0.49}H_{0.68}$ | 380.0 | $53.6 \pm 3.2$ | $1.70 \pm 0.10$ | $1.38 \pm 0.08$ |
| $SiN_{0.65}H_{0.60}$ | 495.0 | $103.0 \pm 4.6$ | $2.69 \pm 0.11$ | $2.18 \pm 0.09$ |
| $SiN_{0.79}H_{0.62}$ | 416.6 | $151.8 \pm 9.0$ | $4.62 \pm 0.27$ | $3.74 \pm 0.22$ |
| $SiN_{0.87}H_{0.93}$ | 486.5 | $210.8 \pm 14.7$ | $5.47 \pm 0.38$ | $4.43 \pm 0.30$ |

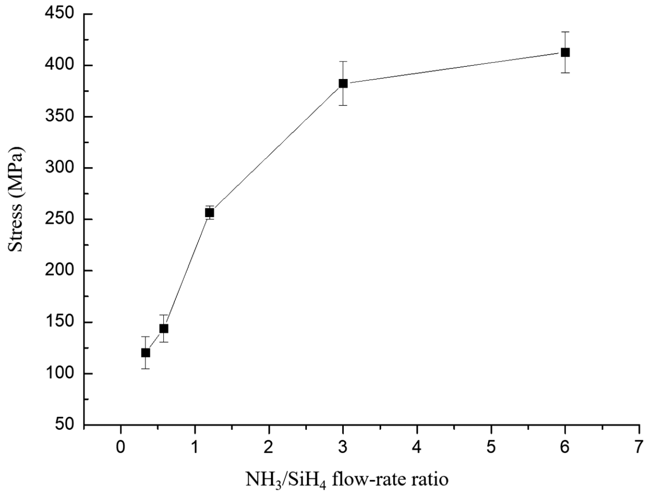

FIG. 7. Tensile stress of the silicon nitride films versus $NH_3/SiH_4$ flow-rate ratio.

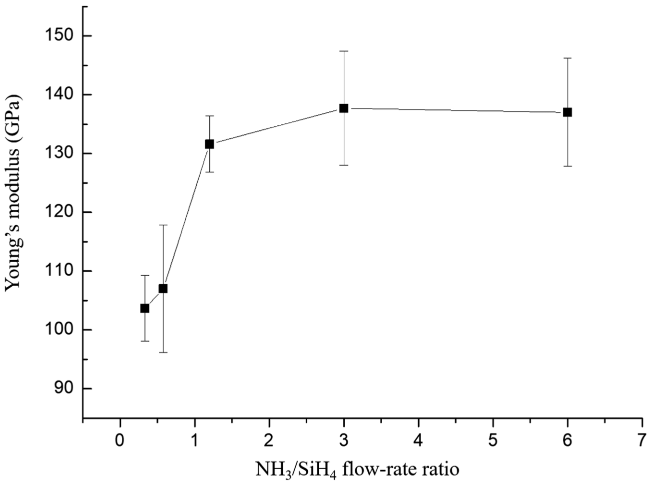

FIG. 8. Young's modulus of the films versus $NH_3/SiH_4$ flow-rate ratio.

An optical curvature meter (KLA Tencor model FLX-2320) was used to measure the curvature of a warped substrate with coating. The Stoney equation [34] was then applied to deduce the stress of the films. Figure 7 shows the stress versus gas flow-rate ratio. The stress was tensile stress, i.e., the coated surface was on the concave side. It ranged from 120 to 410 MPa and increased with increasing $NH_3/SiH_4$ flow-rate ratio. The stresses were smaller than those of the silicon nitride films, ≈2 GPa, produced by the thermally grown LPCVD method [35], which was a high-temperature process above 700°C.

Silicon nitride films are well known to be stressed under various deposition methods and conditions. It was observed and reported that the stress was increased by increasing the flow-rate ratio of $NH_3/SiH_4$, consistent with our observation [36,37]. It was also reported that the stress was diminished by increasing RF power [36,38], implying that a higher deposition rate decreases the stress. The most dominant factor on the stress should be the temperature.

TABLE III. Summary of the optical and mechanical properties of the silicon nitride films.

| $NH_3/SiH_4$ (sccm) | Composition | $n^a$ | $\kappa^a$ ($10^{-5}$) | Eg (eV) | Stress (MPa) | $Y$ (GPa) |
|---|---|---|---|---|---|---|
| 15/45 | $SiN_{0.40}H_{0.79}$ | $2.28 \pm 0.01$ | $1.51 \pm 0.09$ | 2.20 | $120.2 \pm 15.5$ | $103.7 \pm 5.6$ |
| 22/38 | $SiN_{0.49}H_{0.68}$ | $2.12 \pm 0.01$ | $1.70 \pm 0.10$ | 2.41 | $143.8 \pm 13.2$ | $107.0 \pm 10.8$ |
| 30/25 | $SiN_{0.65}H_{0.60}$ | $1.92 \pm 0.01$ | $2.69 \pm 0.11$ | 2.71 | $256.7 \pm 6.6$ | $131.6 \pm 4.8$ |
| 45/15 | $SiN_{0.79}H_{0.62}$ | $1.81 \pm 0.01$ | $4.62 \pm 0.27$ | 4.25 | $382.2 \pm 21.3$ | $137.7 \pm 9.7$ |
| 48/8 | $SiN_{0.87}H_{0.93}$ | $1.78 \pm 0.01$ | $5.47 \pm 0.38$ | 4.83 | $412.7 \pm 20.0$ | $137.0 \pm 9.2$ |

[a] Wavelength at 1550 nm.

High-temperature deposition always produces high-stress film when the thermal expansion coefficients of the film and substrate differ significantly [39,40]. It was also reported that high RF frequency, 13.56 MHz, produced tensile stress, whereas low RF frequency, 380 kHz, produced compressive stress [36,38,39,41].

It is important, therefore, when pairing silicon nitride with other films for the high reflector stack, that the pairing layer have stress at approximately the same level but opposite in sign to avoid accumulating stress in the multilayer stack of the high reflector coatings.

### D. Young's modulus

Young's modulus of the films is related to the thermal noise formulation via the fluctuation-dissipation theorem [42]. Young's modulus of silicon nitride films was measured by using a nanoindenter. The thickness of the films was ≈500 nm so that the surface roughness effect and substrate effect of the nanoindentation measurement were avoided.

Figure 8 shows Young's modulus versus the gas flow-rate ratio. Young's modulus increased from 103 to 137 GPa with increasing $NH_3/SiH_4$ flow-rate ratio. Similar qualitative results were also reported elsewhere [43].

Young's modulus of PECVD silicon nitride films was reported to vary in a wide range, from 85 to 210 GPa, with varied process parameters [35]. Increasing process temperature and RF power can produce films with higher Young's modulus [25].

The aforementioned results are summarized in Table III. It is notable that trends of these quantities are closely correlated with the trend of the nitrogen-to-silicon atomic ratio of the films.

## IV. MECHANICAL LOSS ANGLE MEASUREMENT

### A. Room-temperature ring-down system

We used the cantilever ring-down method to measure the mechanical loss angle. In this method, the cantilever is excited at its resonant frequency $f$, and the damping time $\tau$ is measured to obtain the loss angle $\phi$ and the quality factor $Q$,

$$\phi(f) = \frac{1}{Q} = \frac{1}{\pi f \tau}. \tag{1}$$

The cantilever is held by a clamp. An electrostatic driver is used to excite the cantilever at its resonant frequencies. A laser beam is reflected from the tip of the oscillating cantilever and impinges on a quadrant photodetector. The time-varying oscillation amplitude is then recorded to obtain the time constant of the free damping. The advantage of using the quadrant photodetector is that bending and torsional modes of the cantilever can be distinguished and measured independently [44].

The cantilever was fabricated by using the photolithographic method [45,46]. KOH etching was applied on one surface to thin the cantilever and left a thick pad for clamping. A thicker pad can reduce energy coupling from the cantilever to the clamp [47,48].

Energy coupling between the cantilever and the clamp is the major error source in loss measurement. Given a clamp design, we observed that some modes showed larger coupling than other modes, and the coupling was sensitive to alignment between the cantilever and the clamp, i.e., some modes showed particularly large uncertainty in loss angle upon reclamping. The observation was verified by our simulation result by using COMSOL [49]. In view of this, measurement of those modes was disregarded.

### B. Cryogenic ring-down system

We used a closed-loop cryogenic system, a modified Janis SHI-4XG-15, for cryogenic loss measurement [50]. Liquid helium was recycled between the compressor and the cryostat. A bellows was used to isolate the sample stage from the vibration of the compressor and the displacer. With the bellows design, the root mean square of vibration on the stage was ≈0.1 μm below 40 Hz. The ring-down measurement setup was the same as that of the room-temperature setup, except that the monitor laser was replaced by a 1550-nm laser so that optical absorption by the silicon cantilever was negligible to avoid temperature disturbance [50,51].

For our system, we observed that false loss peaks occurred within the temperature range from ≈150 to 300 K. These peaks could disappear upon reclamping.

For temperatures below ≈100 K, however, no false peaks were ever observed, i.e., the measurements were repeatable below 100 K. The false peaks seemed to be caused by small misalignment and the energy coupling between the clamp and the cantilever. Therefore, we show cryogenic loss data only for the temperature range below 100 K [52].

### C. Loss angle deduction and elastic constant of substrate and films

The loss angle of the substrate $\phi_{\text{sub}}(f)$ and the coated substrate $\phi_{\text{coated}}(f)$ were measured, and the loss angle of the film $\phi_{\text{film}}(f)$ can be deduced as follows:

For bending mode [53,54],

$$\phi_{\text{film}}(f) \approx \frac{Y_s t_s}{3 Y_f t_f} [\phi_{\text{coated}}(f) - \phi_{\text{sub}}(f)]. \tag{2}$$

For torsional mode [55,56],

$$\phi_{\text{film}}(f) \approx \frac{G_s t_s}{3 G_f t_f} [\phi_{\text{coated}}(f) - \phi_{\text{sub}}(f)], \tag{3}$$

where $Y_s$, $Y_f$ are the Young's moduli, $G_s$, $G_f$ are the shear moduli, and $t_s$, $t_f$ are the thickness of the substrate and the film, respectively. These equations are valid only when the elastic energy of the substrate is much larger than that of the film, i.e., substrate is much thicker than the film. Notice that $Y_s$ and $G_s$ are 169 and 79.6 GPa for (100) silicon, respectively [57,58]. $Y_f$ was obtained from Table III. Because the silicon nitride films are amorphous, i.e., homogeneous and isotropic, the shear modulus of the film $G_f$ can therefore be obtained by [59]

$$G_f = \frac{Y_f}{2(1+\nu_f)}, \tag{4}$$

where Poisson's ratio $\nu_f$ was taken to be 0.25 from the literature [60].

Because silicon nitride films are stressed, the coated cantilever warps and the measured loss is inaccurate. Therefore, we coated the silicon cantilever on both sides with identical coating thickness to balance the stress of the sample. The radius of curvature of the double-side coated cantilever was nearly equal to that of the uncoated substrate. The loss angle of the coated cantilever $\phi_{\text{coated}}$ in Eqs. (2) and (3) was modified for the double-side coating accordingly [61].

## V. RESULTS OF MECHANICAL LOSS MEASUREMENT

### A. Room temperature

Figure 9 shows the room-temperature loss angles of the silicon nitride films versus frequency. The first two modes were bending mode and the rest were torsional mode. Losses were near or below the low-$10^{-4}$ range. At ≈100 Hz, the loss decreased with increasing nitrogen content and reached $1.3 \times 10^{-5}$ for $SiN_{0.87}H_{0.93}$.

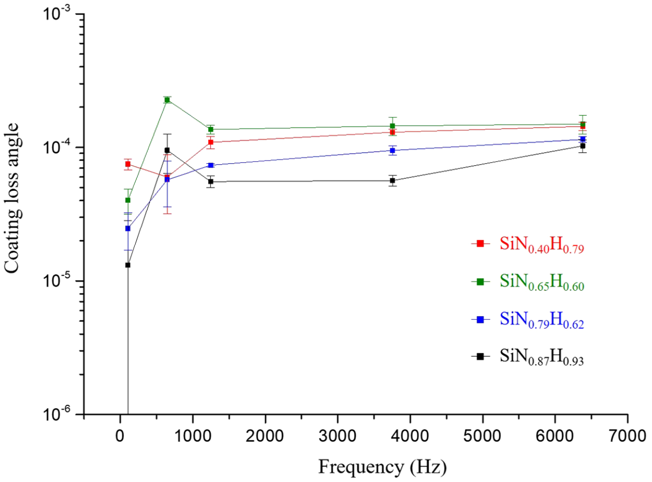

FIG. 9. Room-temperature loss angle of silicon nitride films versus frequency.

The high-index coating for the mirror of the current detector is $Ti:Ta_2O_5$ film, and the room-temperature loss angles of this film were reported to be $2 \times 10^{-4}$ at 55–989 Hz [8] and $2 \times 10^{-4}$ at 60–1100 Hz [62]. Loss angles of the silicon nitride films are lower than or nearly equal to that of the $Ti:Ta_2O_5$ films.

### B. Cryogenic

Figure 10 shows the cryogenic loss angle of the films for two bending modes, 664 and 1854 Hz, and two torsional modes, 1269 and 3845 Hz, respectively. Profound features are clearly observed: $SiN_{0.40}H_{0.79}$ and $SiN_{0.65}H_{0.60}$ did not show loss peaks, and the losses were relatively flat and low; in particular, $5.5 \times 10^{-5}$ for $SiN_{0.40}H_{0.79}$ at low frequency. On the contrary, $SiN_{0.87}H_{0.93}$ and $SiN_{0.79}H_{0.62}$ showed a loss peak at approximately 35 K.

The $Ti:Ta_2O_5$ film for the current detector was reported to have a cryogenic loss peak at 20 K [8], which hinders the application of the film to the next-generation detector operated at cryogenic temperatures. The $SiN_{0.40}H_{0.79}$ and $SiN_{0.65}H_{0.60}$ silicon nitride films are promising in this aspect.

## VI. DISCUSSION

### A. Cryogenic loss

One significant aspect, to our purpose for the next-generation cryogenic detector, of silicon nitride films with various compositions is that the cryogenic mechanical loss peak may or may not exist. In Fig. 11(a), we show the loss angle at 40 K versus $NH_3/SiH_4$ flow ratio extracted from Fig. 10. Figures 11(b) and 11(c) are copies of Fig. 3 for ease of comparison.

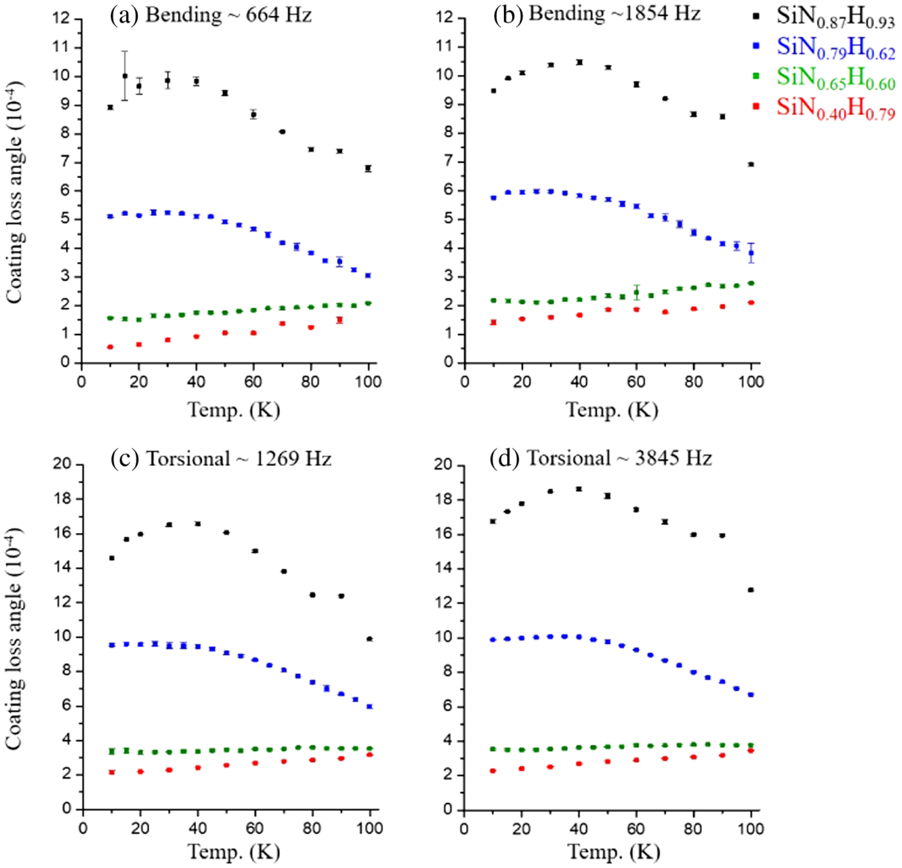

FIG. 10. Cryogenic loss angle of silicon nitride films from 10 to 100 K for bending modes at (a) 664 and (b) 1854 Hz, and torsional modes at (c) 1269 and (d) 3845 Hz.

The bonds between the atoms, rather than the relative number of atoms, are more relevant to the mechanical loss. Figure 11 shows that the increasing cryogenic loss is correlated with increasing N─H bond concentration and decreasing Si─H bond concentration, but is less correlated with the Si─N and Si─Si bond concentration variation. We address the effects associated with the N─H, Si─H, and Si─N bonds to the cryogenic mechanical loss in the following discussion.

We postulate an asymmetrical TLS that associates with the N─H bond and propose that the TLS is the origin of the loss peak at ≈35 K for $SiN_{0.87}H_{0.93}$ and $SiN_{0.79}H_{0.62}$. Figures 12(a) and 12(b) show the molecular structure of $NH_3$ and $SiH_4$, which are the precursors in the PECVD process. Free radicals of these molecules were produced by the RF power to form the plasma in the PECVD process. Consider two possible configurations, referred to as single replacement and double replacement, of the free radical combinations in the solid condensate: a single H of the $NH_3$ is replaced by a Si tetrahedron that is connected to the rest of the amorphous network as shown in Fig. 13(a), and each of two H atoms of the $NH_3$ replaced by a Si tetrahedron that is connected to the rest of the amorphous network as shown in Fig. 14(a). The remaining H and the electron lone pair attached to the nitrogen could exchange position, as shown in Figs. 13(b), 13(c) and 14(b), through phonon-assisted tunneling of the $H^+$, i.e., a single-proton tunneling, thus forming a TLS. The phonon-assisted transition consumes energy of the mechanical oscillation in the amorphous solid and therefore contributes to the mechanical loss. The phonon-assisted proton tunneling was reported for the transitions in the solid of benzoic acid dimer [63,64] and porphine [63,65]. The asymmetrical nature of the TLS arises from the asymmetrical local amorphous environment and the nearby atomic arrangements. The nearby atomic arrangements as viewed along the direction of the N─Si bond are shown in the side plots of Figs. 13(a)–13(c), 14(a) and 14(b). The atoms on the three vertices of the tetrahedrons, shown as $(x, y, z)$ and $(p, q, r)$, could be Si, N, H, and the silicon dangling bond. The arrangement is asymmetrical unless occupancy of all vertices is of the same kind, which is the least likely scenario. It is obvious that the effect is profound for the film possessing high concentration of N─H bonds. Similar to the TLS of the amorphous $SiO_2$ [66,67], the asymmetrical double-well potential of the N─H system can be expressed schematically as shown in Fig. 15, where V refers to the average barrier height. Following the analysis procedure of [8] for $Ta_2O_5$, we identified the location in temperature of the Debye peaks for $SiN_{0.87}H_{0.93}$ at different frequencies from Fig. 10 by

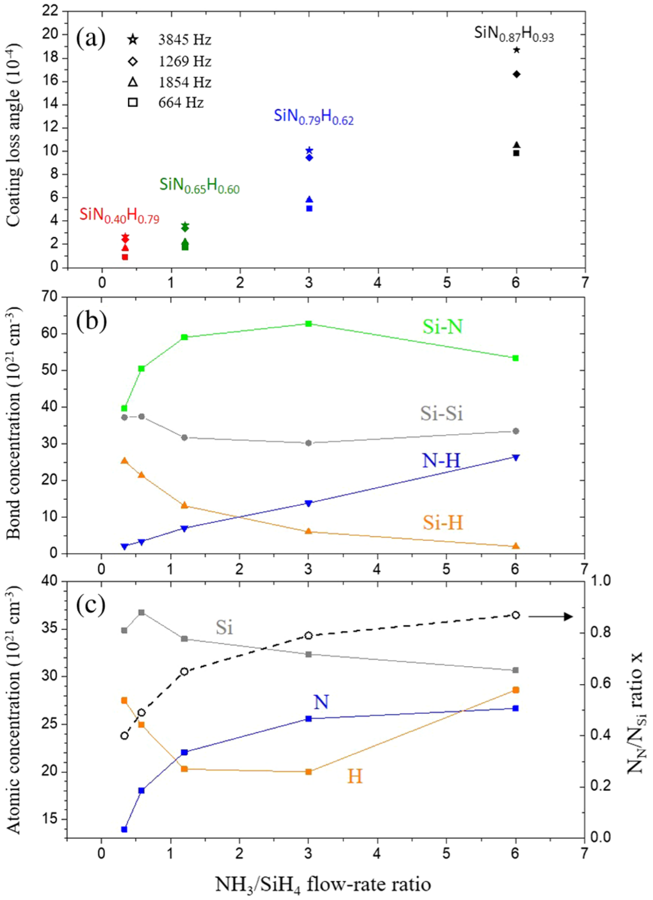

FIG. 11. (a) Loss angle at 40 K for four samples, (b) bond concentration, and (c) atomic concentration versus $NH_3/SiH_4$ flow-rate ratio.

polynomial fitting the peaks; the result is shown in Fig. 16. The activation energy of the TLS associated with the N—H bond, i.e., exchanging position between the $H^+$ and the electron lone pair, was found to be $34.9 \pm 3.4$ meV. The peaks for $SiH_{0.79}H_{0.62}$ are relatively flat and could not be located accurately.

On the other hand, the samples with low $NH_3/SiH_4$ flow ratio, i.e., $SiN_{0.40}H_{0.79}$ and $SiN_{0.65}H_{0.60}$, showed low and flat cryogenic loss with high concentration of Si—H bonds and low concentration of N—H bonds, as shown in Figs. 10 and 11(b). For samples that contain high concentrations of Si—H bonds, we speculate that yet another kind of asymmetrical TLS could exist and contribute to the cryogenic mechanical loss. In Figs. 13(a) and 14(a), H and Si-dangling bonds each could occupy any of the three vertices, $(x, y, z)$ and $(p, q, r)$, of the Si tetrahedron. They are singly connected to the silicon. It is possible that exchanging position of the H atom and the dangling bond through phonon-assisted tunneling of the H atom could occur in this system. Tunneling of the hydrogen atom was reported in hydrogen abstraction reactions in low-temperature solids [68]. However, it was reported that the concentration of the silicon dangling bond $N_{\mathrm{Si}-}$ is approximately 3 orders of magnitude lower than that of the Si—H bond in the PECVD silicon nitride film [18,23]. Therefore, this mechanism is likely to have a minor effect on the cryogenic mechanical loss when there is another mechanism that dominates.

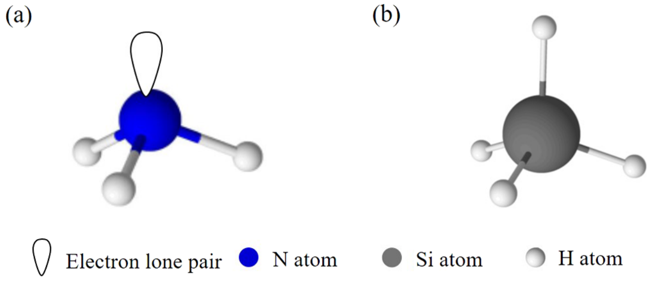

FIG. 12. Molecular structure of (a) $NH_3$ and (b) $SiH_4$.

Yet there is a third possible TLS that is analogous to the well-known ammonia inversion phenomenon [69]; the nitrogen atom together with the lone pair, referring to Figs. 13(a) and 14(a), could also tunnel through the base plane of the nitrogen pyramid, forming a TLS with asymmetrical double-well potential, and the transition is accompanied by the rotation of the nearby Si tetrahedrons similar to what occurs in the transition of the TLS in amorphous $SiO_2$ [66,70]. The potential barrier of the TLS should be high because the ammonia inversion occurs at microwave frequency and the rotation of the nearby Si tetrahedrons adds up to the required energy for the transition. The level of asymmetry, referring to $\Delta$ in Fig. 15, should be high because of the rotation of the nearby tetrahedrons. Therefore, within the frequency range of our interest, this TLS should have little contribution to the cryogenic mechanical loss.

Rigorously speaking, the existence of three-level systems (3LS) cannot be ruled out. For example, a 3LS could exist with the N—H associated exchanging of $H^+$ and electron lone pair when $(x, y, z)$ are all different, referring to Figs. 13(a)–13(c). It could also exist in the Si—H associated exchanging of the H and Si dangling bond when two of the three vertices have the same occupancy that differs from the third, referring to Fig. 14. Exploring the existence and the effects on the mechanical loss of the 3LS is not a trivial task and it relies on loss measurements of higher resolution in temperature and rigorous theoretical modeling [66,71].

In summary, we have proposed three possible TLSs with asymmetrical double-well potential in our material system. The TLSs are associated with N—H, Si—H, and Si—N bonds. The observed cryogenic loss peaks of $SiN_{0.87}H_{0.93}$ and $SiN_{0.79}H_{0.62}$ are believed to be caused by the high concentration of N—H bonds in the film with which an asymmetrical TLS is associated: position exchange between the $H^+$ and the electron lone pair through phonon-assisted tunneling of the single proton associated with the N—H bond forming the TLS. Other TLSs

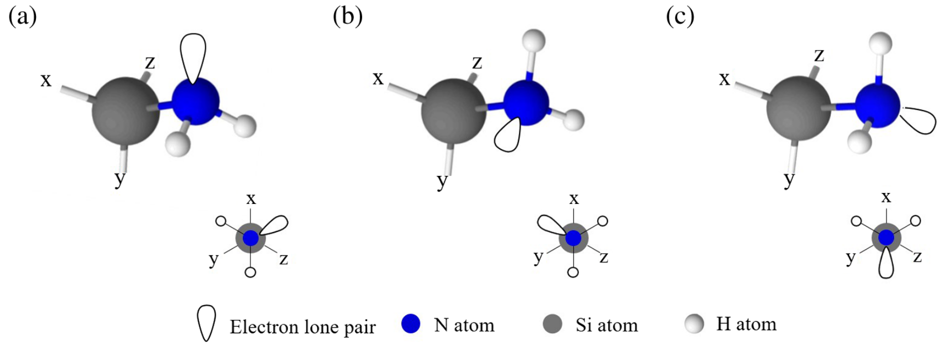

FIG. 13. (a) Single replacement where a single H of the $NH_3$ is replaced by a Si tetrahedron. [(b) and (c)] Configurations of exchanging positions between the $H^+$ and the electron lone pair.

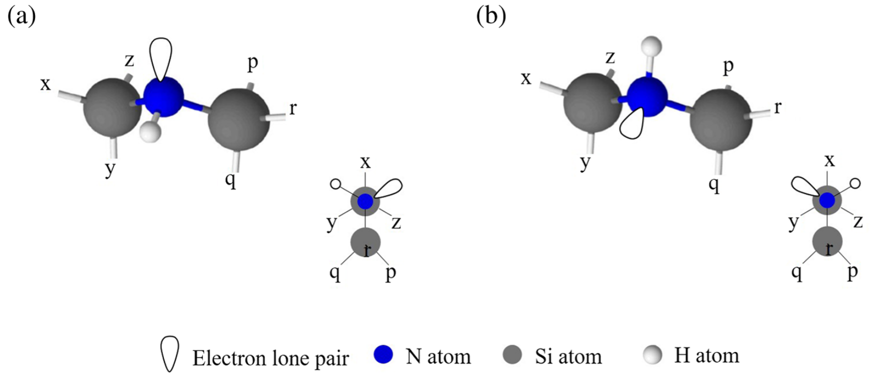

FIG. 14. (a) Double replacement where each of two H atoms of the $NH_3$ is replaced by a Si tetrahedron. (b) Configurations of exchanging positions between the $H^+$ and the electron lone pair.

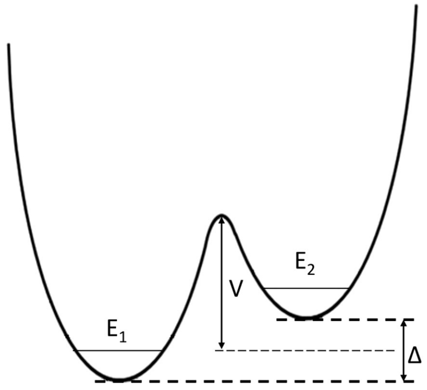

FIG. 15. Schematic of the asymmetrical double-well potential.

associated with the Si─H and Si─N bonds have minor effects on the cryogenic mechanical loss. Experimental evidence in Fig. 11 shows that variation of the cryogenic mechanical loss is highly correlated to the variation of the N─H bond concentration, supporting this hypothesis. We speculate that annealing could be a possible means to change the concentration of the bonds and affect the mechanical loss as well as the optical extinction coefficients.

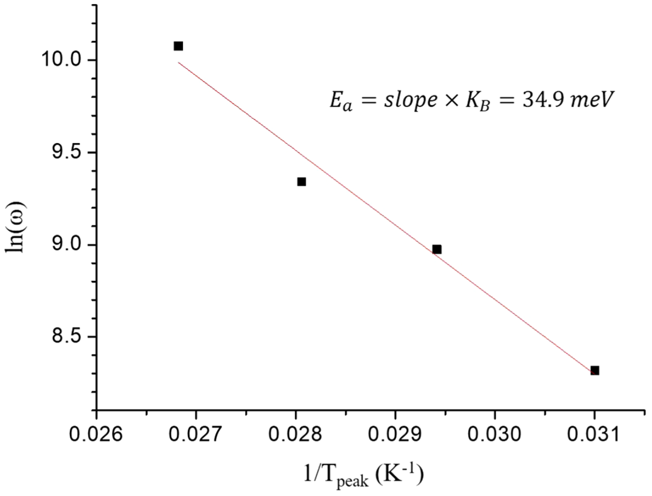

FIG. 16. Arrhenius plot of ln(ω) versus $1/T_{peak}$ for the loss peak of the $SiN_{0.87}H_{0.93}$ film.

### B. Multilayer high reflector stack

High reflector coatings are composed of a quarter-wave (QW) stack with high and low refractive index thin films alternately deposited on the substrate. The requirements for the coatings relevant to the application for the laser

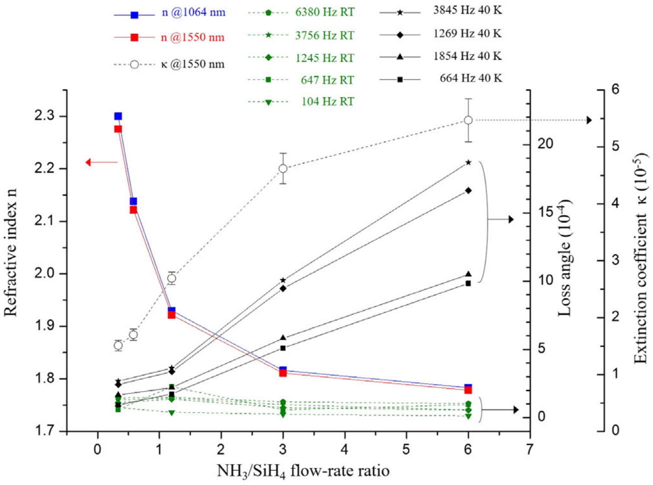

FIG. 17. Refractive index at 1064 (blue squares) and 1550 nm (red squares), extinction coefficient at 1550 nm (hollow circles), and mechanical loss angle at room temperature (green symbols) and 40 K (black symbols) of silicon nitride films versus $NH_3/SiH_4$ flow-rate ratio.

interferometer gravitational wave detector are (1) low optical absorption and scattering, (2) low mechanical loss, (3) large contrast in refractive index, (4) stress match (equal but opposite in sign) between the two thin-film materials, (5) all layers being deposited by the same method in a continuous fashion, and (6) good thickness uniformity for large-area deposition.

We rearranged the data from the previous figures for refractive indices, extinction coefficients, and mechanical loss angles, then replotted them in Fig. 17. The figure clearly shows that the films with low $NH_3/SiH_4$ flow rate, e.g., $SiN_{0.40}H_{0.79}$, have high refractive indices, a large tuning range of refractive indices, low optical extinction coefficients, and low mechanical loss angles, and, in particular, no cryogenic loss peak. The refractive index is higher than that of the $Ti:Ta_2O_5$ film [72], which is used as the high index layer for the coatings of the current advanced-LIGO detector. A higher index implies thinner film and fewer layers are required, hence lower thermal noise, to achieve the same reflectivity. Low cryogenic mechanical loss without a peak outperforms the $Ti:Ta_2O_5$ film that is less suitable for cryogenic applications because of its cryogenic loss peak [8]. Furthermore, the internal tensile stress of films with low $NH_3/SiH_4$ flow rates ranges from +100 to +150 MPa, as shown in Fig. 7, which matches that of the $SiO_2$ film, approximately −150 MPa in compressive stress, deposited by the same PECVD method [73]. The silicon nitride and $SiO_2$ films could be deposited in a continuous load-lock two-chamber PECVD system [74]. These advantages make the $SiN_{0.40}H_{0.79}/SiO_2$ QW stack promising for room- and cryogenic-temperature mirror coatings.

Assuming that the specification for the end-test mass (ETM) of the advanced LIGO at 1064-nm wavelength holds for future detectors at 1550 nm, i.e., 5 ppm for transmittance and <0.5 ppm for absorption [75], we estimated that 14 pairs of $SiN_{0.40}H_{0.79}/SiO_2$ in a QW stack would satisfy the transmission requirement, and the optical absorption loss of the 14-pair QW stack would be 31.4 ppm. There is still room for optical absorption reduction. Thermal annealing could be a direction to reduce the optical absorption of the silicon nitride film in the future. Alternatively, multimaterial coatings [76] could be designed that incorporate the film with high optical absorption and low mechanical loss with the film with low optical absorption but high mechanical loss into the QW stack. It is notable that the optical absorption of the $SiN_{0.40}H_{0.79}$ film is lower than that of the IBS-deposited amorphous silicon film [32,33] that is a potential candidate material for the high index layer in the coating of the future detector.

## VII. CONCLUSION

We showed that amorphous silicon nitride films with different compositions could be deposited by using the PECVD method. Thorough investigations were performed to study the physical properties of the films that are pertinent to the application of the mirror coatings for the laser interferometer gravitational wave detector. We measured the refractive index, optical extinction coefficient, energy gap, stress, Young's modulus, room-temperature and cryogenic mechanical loss of the films and found correlations of these quantities with the composition and bond concentrations variations of the films. Optical extinction coefficients of the as-deposited films were in the $10^{-5}$ range at 1550 nm, lower than that of the IBS as-deposited amorphous silicon film [32,33]. Room-temperature mechanical loss values were in the low-$10^{-4}$ to $10^{-5}$ range, lower than the $Ti:Ta_2O_5$ of the current coating for the gravitational wave detector. $SiN_{0.40}H_{0.79}$ and $SiN_{0.65}H_{0.60}$ films, which had low N─H bond concentration, did not show cryogenic loss peaks, a promising feature in contrast to the $Ti:Ta_2O_5$ coating for the current detector. TLS of exchanging positions between the $H^+$ and the electron lone pair associated with the N─H bond is the source of the observed cryogenic loss peak for the silicon nitride films that contain high concentrations of N─H bonds. It is feasible that amorphous silicon nitride films deposited by the PECVD method, with its range of refractive index and stress, could be used to pair with either high or low refractive index films, such as amorphous silicon [77,78] or $SiO_2$, to form the QW stack of the high reflector by the all-PECVD deposition method.

## ACKNOWLEDGMENTS

The work of this study was supported by the Ministry of Science and Technology of Taiwan, the Republic of China, under Contract No. 103-2221-E-007-064-MY3. The authors appreciate the comments from the Optics Working Group of the LIGO Scientific Collaboration.

[1] B. P. Abbott *et al.* (LIGO Scientific Collaboration and Virgo Collaboration), Observation of Gravitational Waves from a Binary Black Hole Merger, Phys. Rev. Lett. **116**, 061102 (2016).

[2] LIGO Scientific Collaboration, Instrument Science White Paper LIGO—T1600119-v4, 2016, https://dcc-backup.ligo.org/LIGO-T1600119/public.

[3] H. B. Callen and T. A. Welton, Irreversibility and generalized noise, Phys. Rev. **83**, 34 (1951).

[4] J. Aasi *et al.* (LIGO Scientific Collaboration), Advanced LIGO, Classical Quantum Gravity **32**, 074001 (2015).

[5] ET Science Team, Einstein gravitational wave telescope conceptual design study: ET-0106C-10 (European gravitational observatory, Cascina Italy, 2011), p. 376.

[6] B. Sassolas *et al.*, Mitigation of the spiral pattern induced by the planetary motion, in *OSA Technical Digest (Online)* (Optical Society of America, 2016), paper MB.6.

[7] C. Michel, N. Morgado, L. Pinard, B. Sassolas, R. Bonnand, J. Degallaix, D. Forest, and R. Flaminio, Realization of low-loss mirrors with sub-nanometer flatness for future gravitational wave detectors, Proc. SPIE Int. Soc. Opt. Eng. **8550**, 85501P (2012).

[8] I. W. Martin *et al.*, Measurements of a low-temperature mechanical dissipation peak in a single layer of $Ta_2O_5$ doped with $TiO_2$, Classical Quantum Gravity **25**, 055005 (2008).

[9] I. W. Martin *et al.*, Low temperature mechanical dissipation of an ion-beam sputtered silica film, Classical Quantum Gravity **31**, 035019 (2014).

[10] R. Nawrodt *et al.*, High mechanical Q-factor measurements on silicon bulk samples, J. Phys. Conf. Ser. **122**, 012008 (2008).

[11] D. R. Southworth, R. A. Barton, S. S. Verbridge, B. Ilic, A. D. Fefferman, H. G. Craighead, and J. M. Parpia, Stress and silicon nitride: A crack in the universal dissipation of glasses, Phys. Rev. Lett. **102**, 225503 (2009).

[12] D. L. Smith, A. S. Alimonda, C. C. Chen, S. E. Ready, and B. Wacker, Mechanism of $SiN_xH_y$ deposition from $NH_3 - SiH_4$ plasma, J. Electrochem. Soc. **137**, 614 (1990).

[13] N. Jehanathan, M. Saunders, Y. Liu, and J. Dell, Crystallization of silicon nitride thin films synthesized by plasma-enhanced chemical vapour deposition, Scr. Mater. **57**, 739 (2007).

[14] W. R. Knolle and J. W. Osenbach, The structure of plasma-deposited silicon nitride films determined by infrared spectroscopy, J. Appl. Phys. **58**, 1248 (1985).

[15] M. H. Brodsky, M. Cardona, and J. J. Cuomo, Infrared and Raman spectra of the silicon-hydrogen bonds in amorphous silicon prepared by glow discharge and sputtering, Phys. Rev. B **16**, 3556 (1977).

[16] H. Shanks, C. J. Fang, L. Ley, M. Cardona, F. J. Demond, and S. Kalbitzer, Infrared spectrum and structure of hydrogenated amorphous silicon, Phys. Status Solidi **100**, 43 (1980).

[17] C. J. Fang, K. J. Gruntz, L. Ley, M. Cardona, F. J. Demond, G. Muller, and S. Kalbitzer, The hydrogen content of a-Ge:H and a-Si:H as determined by IR spectroscopy, gas evolution and nuclear reaction techniques, J. Non-Cryst. Solids **35–36**, 255 (1980).

[18] A. Morimoto, Y. Tsujimura, M. Kumeda, and T. Shimizu, Properties of hydrogenated amorphous Si-N prepared by various methods, Jpn. J. Appl. Phys. **24**, 1394 (1985).

[19] G. Sasaki, M. Kondo, S. Fujita, and A. Sasaki, Properties of chemically vapor-deposited amorphous $SiN_x$ alloys, Jpn. J. Appl. Phys. **21**, 1394 (1982).

[20] M. M. Guraya, H. Ascolani, G. Zampieri, J. I. Cisneros, J. H. DiasdaSilva, and M. P. Cantao, Bond densities and electronic structure of amorphous $SiN_x$ : H, Phys. Rev. B **42**, 5677 (1990).

[21] T. Makino and M. Maeda, Bonds and defects in plasma-deposited silicon nitride using $SiH_4$-$NH_3$-Ar mixture, Jpn. J. Appl. Phys. **25**, 1300 (1986).

[22] V. Verlann, A. D. Verkerk, W. M. Arnoldbik, C. H. M. van der Werf, R. Bakker, Z. S. Houweling, I. G. Romijn, D. M. Borsa, A. W. Weeber, S. L. Luxembourg, M. Zeman, H. F. W. Dekkers, and R. E. I. Schropp, The effect of composition on the bond structure and refractive index of silicon nitride deposited by HWCVD and PECVD, Thin Solid Films **517**, 3499 (2009).

[23] D. Jousse, J. Kanicki, D. T. Krick, and P. M. Lenahan, Electron-spin-resonance study of defects in plasma-enhanced chemical vapor deposited silicon nitride, Appl. Phys. Lett. **52**, 445 (1988).

[24] N. Jehanathan, Y. Liu, B. Walmsley, J. Dell, and M. Saunders, Effect of oxidation on the chemical bonding structure of PECVD $SiN_x$ thin films, J. Appl. Phys. **100**, 123516 (2006).

[25] H. Huang, K. J. Winchester, A. Suvorova, B. Lawn, Y. Liu, X. Z. Hu, J. M. Dell, and L. Faraone, Effect of deposition conditions on mechanical properties of low-temperature PECVD silicon nitride films, Mater. Sci. Eng. A **435–436**, 453 (2006).

[26] G. E. Jellison, Jr. and F. A. Modine, Parameterization of the optical functions of amorphous materials in the interband region, Appl. Phys. Lett. **69**, 371 (1996).

[27] J. Tauc, in *Optical Properties of Solids*, edited by S. Nudelman and S. S. Mitra (Olenum, New York, 1969), p. 123.

[28] A. Alexandrovski, M. Fejer, A. Markosyan, and R. Route, Photothermal common-path interferometry (PCI): new developments, in *Proceedings of SPIE 7193, Solid State Lasers XVIII: Technology and Devices* (San Jose, 2009), p. 71930D.

[29] F. Urbach, The long-wavelength edge of photographic sensitivity and of the electronic absorption of solids, Phys. Rev. **92**, 1324 (1953).

[30] J. Tauc, States in the gaps, J. Non-Cryst. Solids **8–10**, 569 (1972).

[31] M. H. Cohen, Review of the theory of amorphous semiconductors, J. Non-Cryst. Solids **4**, 391 (1970).

[32] J. Steinlechner, I. W. Martin, R. Bassiri, A. Bell, M. M. Fejer, J. Hough, A. Markosyan, R. K. Route, S. Rowan, and Z. Tornasi, Optical absorption of ion-beam sputtered amorphous silicon coatings, Phys. Rev. D **93**, 062005 (2016).

[33] J. Steinlechner, A. Khalaidovski, and R. Schnabel, Optical absorption measurement at 1550 nm on a highly-reflective $Si/SiO_2$ coating stack, Classical Quantum Gravity **31**, 105005 (2014).

[34] G. G. Stoney, The tension of metallic films deposited by electrolysis, Proc. R. Soc. A **82**, 172 (1909).

[35] A. Stoffel, A. Kovács, W. Kronast, and B. Muller, LPCVD against PECVD for micromechanical applications, J. Micromech. Microeng. **6**, 1 (1996).

[36] C. Iliescu, F. E. H. Tay, and J. Wei, Low stress PECVD—SiNx layers at high deposition rates using high power and high frequency for MEMS applications, J. Micromech. Microeng. **16**, 869 (2006).

[37] K. D. Mackenzie, D. J. Johnson, M. W. DeVre, R. J. Westerman, and B. H. Reelfs, Stress control of Si-based PECVD dielectrics, in *207th Electrochemical Society Meeting PV2005-01* (Electrochemical Society, Quebec City Canada, 2005), p. 148.

[38] A. Bagolini, A. S. Savoia, A. Picciotto, M. Boscardin, P. Bellutti, N. Lamberti, and G. Caliano, PECVD low stress silicon nitride analysis and optimization for the fabrication of CMUT devices, J. Micromech. Microeng. **25**, 015012 (2015).

[39] W. A. P. Claassen, W. G. J. N. Valkenburg, M. F. C. Willemsen, and W. M. V. D. Wijgert, Influence of deposition temperature, gas pressure, gas phase composition, and RF frequency on composition and mechanical stress of plasma silicon nitride layers, J. Electrochem. Soc. **132**, 893 (1985).

[40] K. Allaert, A. V. Calster, H. Loos, and A. Lequesne, comparison between silicon nitride films made by PCVD of $N_2$-$SiH_4$/Ar and $N_2$-$SiH_4$/He, J. Electrochem. Soc. **132**, 1763 (1985).

[41] D. W. Hess, Plasma-enhanced CVD: Oxides, nitrides, transition metals, and transition metal silicides, J. Vac. Sci. Technol. A **2**, 244 (1984).

[42] G. M. Harry *et al.*, Thermal noise in interferometric gravitational wave detectors due to dielectric optical coatings, Classical Quantum Gravity **19**, 897 (2002).

[43] J. A. Taylor, The mechanical properties and microstructure of plasma enhanced chemical vapor deposited silicon nitride thin films, J. Vac. Sci. Technol. A **9**, 2464 (1991).

[44] W. Y. Wang, Master's thesis, NTHU Hsinchu Taiwan, 2013.

[45] S. Chao *et al.*, LIGO Report No. LIGO-G1200849, 2012, https://dcc.ligo.org/LIGO-G1200849/public.

[46] R. Nawrodt, Investigation of mechanical losses of thin silicon flexures at low temperatures, Classical Quantum Gravity **30**, 115008 (2013).

[47] T. Quinn, C. Speake, R. Davis, and W. Tew, Stress-dependent damping in Cu-Be torsion and flexure suspensions at stresses up to 1.1 GPa, Phys. Lett. A **197**, 197 (1995).

[48] S. Reid, G. Cagnoli, D. R. M. Crooks, J. Hough, P. Murray, S. Rowan, M. M. Fejer, R. Route, and S. Zappe, Mechanical dissipation in silicon flexures, Phys. Lett. A **351**, 205 (2006).

[49] H. W. Pan, H. C. Chen, L. C. Kuo, and S. Chao, LIGO Report No. LIGO-G1700299, 2017, https://dcc.ligo.org/LIGO-G1700299/public.

[50] S. Chao, L. C. Kuo, H. W. Pan, C. Cheng, and S. Y. Huang, LIGO Report No. LIGO-G1501048, 2015, https://dcc.ligo.org/LIGO-G1501048/public.

[51] C. Cheng, Master's thesis, NTHU Hsinchu Taiwan, 2015.

[52] L. C. Kuo, H. W. Pan, H. Wu, H. Y. Ho, and S. Chao, LIGO Report No. LIGO-G1700301, 2017, https://dcc.ligo.org/LIGO-G1700301/public.

[53] B. Berry and W. C. Pritchet, Vibrating reed internal friction apparatus for films and foils, IBM J. Res. Dev. **19**, 334 (1975).

[54] A. Heptonstall, G. Cagnoli, J. Hough, and S. Rowan, Characterisation of mechanical loss in synthetic fused silica ribbons, Phys. Lett. A **354**, 353 (2006).

[55] B. E. White, Jr. and R. O. Pohl, Internal Friction of Subnanometer $a$-$SiO_2$ Films, Phys. Rev. Lett. **75**, 4437 (1995).

[56] X. Liu, B. E. White, Jr., R. O. Pohl, E. Iwanizcko, K. M. Jones, A. H. Mahan, B. N. Nelson, R. S. Crandall, and S. Veprek, Amorphous Solid Without Low Energy Excitations, Phys. Rev. Lett. **78**, 4418 (1997).

[57] M. A. Hopcroft, W. D. Nix, and T. W. Kenny, What is the Young's modulus of silicon?, J. Microelectromech. Syst. **19**, 229 (2010).

[58] J. J. Wortman and R. A. Evans, Young's modulus, shear modulus, and Poisson's ratio in silicon and germanium, J. Appl. Phys. **36**, 153 (1965).

[59] L. D. Landau and E. M. Lifshitz, in *Theory of Elasticity*, 3rd ed. (Pergamon, Oxford, 1986), p. 13.

[60] B. A. Walmsley, Y. Liu, X. Z. Hu, M. B. Bush, J. M. Dell, and L. Faraone, Poisson's ratio of low-temperature PECVD silicon nitride thin films, J. Microelectromech. Syst. **16**, 622 (2007).

[61] S. Chao, H. W. Pan, S. Y. Huang, and L. C. Kuo, LIGO Report No. LIGO-G1501068, 2015, https://dcc.ligo.org/LIGO-G1501068/public.

[62] R. Flaminio, J. Franc, C. Michel, N. Morgado, L. Pinard, and B. Sassolas, A study of coating mechanical and optical losses in view of reducing mirror thermal noise in gravitational wave detectors, Classical Quantum Gravity **27**, 084030 (2010).

[63] T. Sugawara and I. Takasu, in *Adavnces in Physical Orgenic Chemisty*, edited by D. Bethell (Academic press, San Diego, 1999), Vol. 32, p. 219.

[64] A. Stöckli, B. H. Meier, R. Kreis, R. Meyer, and R. R. Ernst, Hydrogen bond dynamics in isotopically substituted benzoic acid dimers, J. Chem. Phys. **93**, 1502 (1990).

[65] K. M. Merz, Jr. and C. H. Reyno1ds, Tautomerism in free base porphyrins: The porphyrin potential energy surface, J. Chem. Soc., Chem. Commun. **0**, 90 (1988).

[66] R. Hamdan, J. P. Trinastic, and H. P. Cheng, Molecular dynamics study of the mechanical loss in amorphous pure and doped silica, J. Chem. Phys. **141**, 054501 (2014).

[67] W. A. Phillips, Tunneling states in amorphous solids, J. Low Temp. Phys. **7**, 351 (1972).

[68] R. Le Roy, H. Murai, and F. Williams, Tunneling model for hydrogen abstraction reactions in low-temperature solids. Applications to reactions in alcohol glasses and acetonitrile crystals, J. Am. Chem. Soc. **102**, 2325 (1980).

[69] C. E. Cleeton and N. H. Williams, Electromagnetic waves of 1.1 cm wave-length and the absorption spectrum of ammonia, Phys. Rev. **45**, 234 (1934).

[70] U. Buchenau, N. Nucker, and A. J. Dianoux, Neutron Scattering Study of the Low-Frequency Vibrations in Vitreous Silica, Phys. Rev. Lett. **53**, 2316 (1984).

[71] J. P. Trinastic, R. Hamdan, Y. Wu, L. Zhang, and H. P. Cheng, Unified interatomic potential and energy barrier distributions for amorphous oxides, J. Chem. Phys. **139**, 154506 (2013).

[72] J. Steinlechner, C. Kruger, I. W. Martin, A. Bell, J. Hough, H. Kaufer, S. Rowan, R. Schnabel, and S. Steinlechner, Optical absorption of silicon nitride membranes at 1064 nm and at 1550 nm, Phys. Rev. D **96**, 022007 (2017).

[73] H. W. Pan, Z. Z. Xie, L. C. Kuo, and S. Chao, LIGO Report No. LIGO-G1500194, 2015, https://dcc.ligo.org/LIGO-G1500194/public.

[74] S. Chao, H. W. Pan, L. C. Kuo, S. Y. Huang, M. Y. Wu, Y. H. Juang, and C. W. Lee, LIGO Report No. LIGO-G1601298, 2016, https://dcc.ligo.org/LIGO-G1601298/public.

[75] G. Billingsley, LIGO Report No. LIGO-E0900068, 2014, https://dcc.ligo.org/LIGO-E0900068/public.

[76] J. Steinlechner, I. W. Martin, J. Hough, C. Kruger, S. Rowan, and R. Schnabel, Thermal noise reduction and absorption optimization via multimaterial coatings, Phys. Rev. D **91**, 042001 (2015).

[77] X. Liu, C. L. Spiel, R. O. Pohl, E. Iwaniczko, and R. S. Crandall, Low temperature internal friction study of light-induced structural instability in hydrogenated amorphous silicon, J. Non-Cryst. Solids **266–269**, 501 (2000).

[78] X. Liu, C. L. Spiel, R. D. Merithew, R. O. Pohl, B. P. Nelson, Q. Wang, and R. S. Crandall, Internal friction of amorphous and nanocrystalline silicon at low temperatures, Mater. Sci. Eng. A **442**, 307 (2006).